Contents lists available at ScienceDirect

Journal of Pipeline Science and Engineering

Computational fluid dynamics driven mass transfer model for the prediction of CO_2 corrosion in pipelines

Udayraj Thorat [*], Michael Jones, Richard Woollam, Joshua Owen, Richard Barker, Harvey Thompson, Gregory de Boer

School of Mechanical Engineering, University of Leeds, Leeds LS2 9JT, UK

ABSTRACT

A novel, computational fluid dynamics (CFD) driven modelling methodology for predicting CO_2 corrosion rates in pipelines is presented. CFD is used to provide accurate predictions of the viscous sublayer thickness and turbulent diffusivities, which are then used within a mass transfer model of aqueous CO_2 corrosion. Comparisons with experimental measurements of corrosion rate in horizontal pipe flow and corresponding theoretical predictions, based on empirical correlations and previous CFD approaches, show the new approach is more accurate for flows in the range of pH 4 to 6. However, the key advantage of the new approach is its flexibility. Existing models are inaccurate and highly restrictive, having been derived for very simple cases, such as 1 D pipe flow. In contrast, the new methodology provides a firm, scientific foundation for predicting corrosion rates by determining conditions in the viscous sublayer in much more complex, and practically relevant, flow situations.

1. Introduction

Aqueous CO_2 corrosion, occurs when CO_2 gas dissolves in water to form carbonic acid (H_2CO_3), observed in industries such as oil and gas, petrochemical, and power generation. There are several empirical (Olsen, 2003; Halvorsen and Sontvedt, 1999), semi-empirical (de Waard and Milliams, 1975; de Waard et al., 2003), elementary mechanistic (Gray et al., 1989; Nešić et al., 2009; Nesic et al., 1995; Nordsveen et al., 2003; Nesic et al., 2001), and comprehensive mechanistic models (Nešić et al., 2019; Kahyarian and Nesic, 2020) that are now available for the prediction of CO_2 corrosion in single-phase pipeline flow. The mechanistic models available have extended their scope by adding complexity, such as the effect of multiphase flow (Nešić et al., 2019), the impact of protective corrosion product formation (Nordsveen et al., 2003; Nesic et al., 2001), and other corrosive species into these models (Kahyarian and Nesic, 2020; Zheng, 2015). Some approaches include combinations of experimental work with theoretical modelling for investigating the impact of surface roughness (Al-Khateeb et al., 2018) and rapid expansion geometry (Owen et al., 2019) upon which the current work is based.

The flow in a pipeline is characterised as laminar, transitional, or turbulent based on the Reynolds number (Re). The flow field in most of the mechanistic models is assumed as turbulent due to high flow rate and length of the pipes used for transportation (Kahyarian and Nesic, 2020; Nesic et al., 1995; Nešić et al., 2019; Nordsveen et al., 2003; Zheng, 2015; Nešić et al., 2009; Nesic et al., 2001), resulting in a fully developed turbulent flow (Nešić, 2007). This flow field is divided into three regions: the viscous sublayer (VSL), the buffer layer, and the turbulent layer, as shown in Fig. 1.

Very close to the wall, mass transfer is dominated by molecular diffusion. However, studies related to the observation of fluid elements adjacent to the wall have shown that vertical components of velocity fluctuations continue to exist until they reach the wall and thus occur within the VSL of a turbulent flow (Popovich and Hummel, 1967). The effect of turbulent convection on an element carried within the fluid can be quantified using the notion of turbulent diffusivity (D_t). The dispersion of particles in a given region is caused by eddies within the fluid flow. These eddies cascade in scale down to a size smaller than that of the region; larger eddies advect the fluid region but do not cause element separation. As the region grows in size due to advection, the range of eddies captured facilitates the dispersion of particles in the flow. This is turbulent diffusion, different from eddy diffusion, which is the process by which eddies are dispersed in a turbulent flow. The available equations for measuring turbulent behaviour are based on steady-state approximations since capturing the time-dependant behaviour of turbulence without an experiment for a particular flow is highly
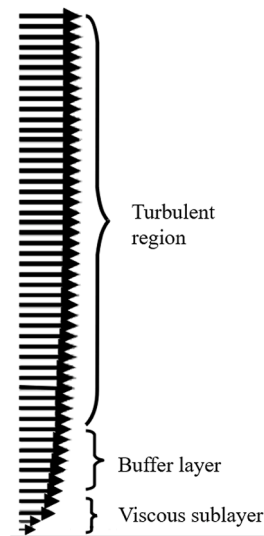
Fig. 1. Turbulent boundary layer profile over a flat plate (not to scale).

challenging. Hence, the time-dependant fluid flow and mass transport changes are described using eddy and turbulent diffusivity, respectively. As a result, researchers have no consensus on predicting turbulent diffusivity in horizontal pipelines. All empirical equations for the turbulent diffusivity are either assumed in a general form (Notter and Sleicher, 1971) or obtained by experimental data fitting (Nordsveen et al., 2003; Notter and Sleicher, 1971; Davies, 1972; Wang and Nesic, 2003). These empirical correlations are only applicable for a fully developed pipe flow, limiting their use in non-idealised geometries such as elbows, rectangular channels, or sudden expansion/constriction. This has become one of the main drawbacks of using empirical correlations in the mechanistic modelling of CO_2 corrosion, which the present study aims to alleviate using CFD to determine the turbulent boundary layer profile and flow behaviour in the near wall region.

CFD is a reliable methodology for obtaining a discrete solution for fluid flow in real-life engineering applications (Yeoh and Tu, 2010). There has been a significant increase in the use of CFD modelling for corrosion or erosion-corrosion prediction models over the last couple of decades. In elbows, CFD has been used to predict hydrodynamic flow fields and then coupled to the erosion-corrosion model to determine the significance of bend orientation (Keating and Nesic, 2000) and flow velocity (Bozzini et al., 2003) in multiphase flows. Flow accelerated corrosion (FAC) has been studied using both experimental and CFD techniques at $Re = 40,000$ (El-Gammal et al., 2010) to explore the importance of parameters such as surface roughness, wall shear stress, upstream turbulence, and the role of geometry on the prediction of local mass transfer coefficients (Pietralik, 2012). CFD was found to be helpful in providing correlations for mass transfer coefficient at higher Reynolds numbers when the empirical equations were not available (Pietralik, 2012).

In pipeline flows, CFD simulations are used for understanding the mechanism of slug flow-induced CO_2 corrosion (Zheng et al., 2007; Lv et al., 2020), to predict erosion failure positions in the multiphase flow (Tang et al., 2009) and in understanding the effect of the impact angle on the corrosion of the steel in the study of FAC of X65 pipeline steel using an impingement jet test system in CO_2-saturated formation water (Zhang and Cheng, 2010). CFD located the most probable corrosion sites based on water volume fraction (El-Batsh et al., 2012) and water accumulating regions (Hu and Cheng, 2016). Some studies (Hu and Cheng, 2016; Li et al., 2016) predicted CO_2 corrosion rates using CFD based on empirical (Kanwar, 1994) and semi-empirical corrosion models (Jepson et al., 1996). Prasad et al. (2018) coupled the mechanistic model (Sanchez-Caldera et al., 1988) and CFD to predict FAC by considering the

reduction in wall thickness. The mass transfer coefficient (MTC) in their study was computed using CFD in bend and orifice geometries. Li and Woollam (2012) used CFD along with a mechanistic model to predict corrosion rates in sharp bend geometry of disturbed flow. They found that highest values of corrosion rates near the bend as the mass transfer experienced was maximum. Wang et al. (2022) studied the water-wetting conditions in gas-water two-phase flow in natural gas pipelines using CFD, which they then coupled with a corrosion model to check the effect on FAC with the changes in fluid velocity and elbow angle on the wall shear stress.

Wang (1999) coupled the fluid flow model with a numerical model for the prediction of CO_2 corrosion in pipelines. The corrosion rate predictions were based on mixed potential theory, and the straight pipe correlation of Berger and Hau (1977) was used for overall MTCs in a simplified electrochemical model. Although an attempt was made to couple the flow and electrochemical models, the corrosion rate predictions showed discrepancies upon comparison with experimental data. It has been assumed that the VSL exists either at $y^+ < 5$ (Wang, 1999) or $y^+ = 5$ (Wang et al., 2020) without the accurate coupling of fluid flow model. Some of the recent research include the prediction of CO_2 corrosion in straight pipe and jet impingement using CFD which over-predicted corrosion rates (Hu et al., 2018; Srinivasan, 2015). Hu et al. (2018) used the Abe-Kondoh-Nagano k-ε turbulence model (Abe et al., 1994) for the fluid flow simulations with different sets of electrochemical reaction rate constants in the mass transfer model. This underlines the fact there is a lack of methodology which accurately predicts the VSL thickness and turbulent diffusivity profile and then subsequently couples it to the mass transfer model of CO_2 corrosion rate.

The CFD-driven corrosion prediction model in this study provides a robust approach for coupling fluid flow and mass transfer models for the prediction of corrosion rates. A key feature of this approach is the accurate calculation of the VSL thickness and turbulent diffusivity profiles which sets a benchmark for the corrosion rate predictions in disturbed, developing and fully developed flow conditions. The mass transfer model is based on the Nordsveen et al. (2003) multi-node model, which integrates the species transport equations through the VSL to calculate the concentration of each species at a series of points by accounting for the transport of species to and from the bulk. It includes homogeneous chemical reactions, diffusion of species, electrochemical reactions at the steel surface and transport of species to and from the bulk, including diffusion and convection through the VSL (Nordsveen et al., 2003). Section 2 describes the mass transfer, velocity and eddy distribution in pipeline flows and CFD methodology. Section 3 presents a comprehensive series of results containing the calculations of the VSL thickness, turbulent diffusivities, corrosion rates and verification with the experimental and numerical data in the relevant literature.

2. Materials and methods

2.1. Mass transfer modelling

Species' transport is described using species conservation equations. The governing equation for the transport of diluted species j in a fluid medium is given by Eq. (1):

$$\frac{\partial c_j}{\partial t} = -\frac{\partial N_j}{\partial x} + R_j \tag{1}$$

Where c_j is the concentration of species j, N_j is the flux of species j due to diffusion, R_j is the rate of production of species j due to homogeneous chemical reactions, t is the time, and x is the spatial coordinate (distance from the metal surface). Fig. 2 shows the transport of species in the mass transfer model.

The flux of species N_j is made up of contributions from diffusion, electro-migration, and convection. The model developed here is applied to cases where the electrolytes have high conductivity, including the
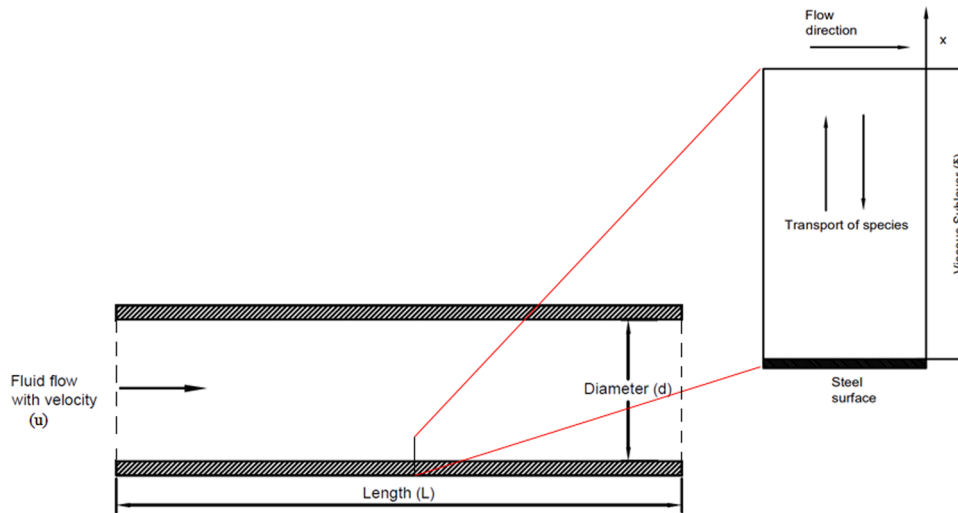
Fig. 2. Transport of species in mass transfer modelling in horizontal pipelines.

major species Na^+ and Cl^-, with the result that electro-migration in the electric field is negligible compared to diffusion and convection. For a comprehensive justification of this assumption, see references (Balsara and Newman, 2021; Stephens and Mauzeroll, 2019). In addition, since the aim is to assess the importance of modelling the VSL accurately on corrosion modelling, the model is developed for cases where the precipitation of $FeCO_3$ is negligible, obviating the need for introducing additional empiricism into the corrosion modelling, as in previous models for corrosion product formation, see e.g., Nesic et al., 2001. In fact, in the cases considered here, the temperatures are very low (around 20 °C), which means that the super-saturation S given by Eq. (2):

$$S = \frac{c_{Fe^{2+}} c_{CO_3^{2-}}}{K_{sp}} \qquad (2)$$

is small, and the precipitation of $FeCO_3$ will therefore be negligible. This issue is discussed in greater detail by Nesic et al. (2001) who concluded that the precipitation rate of $FeCO_3$ is extremely low for temperatures less than 60 °C. The ability to neglect corrosion product formation enables a steady-state modelling approach to be adopted.

The flux of species N_j is given by Eq. (3):

$$N_j = -\left(D_j + D_t\right) \frac{\partial c_j}{\partial x} \qquad (3)$$

Where D_j is the molecular diffusivity of species j, and D_t is turbulent diffusivity for all species.

The turbulent diffusivity (D_t) is shown by Eq. (4):

$$D_t = \frac{\mu_T}{\rho Sc_t} \qquad (4)$$

Where μ_T is the turbulent viscosity and Sc_t is the turbulent Schmidt number with an approximate value ranging from 0.5 to 0.9, which requires calibration for a specific problem (Tominaga and Stathopoulos, 2007). The sensitivity of the term Sc_t to corrosion rate predictions by varying it from 0.5 to 0.9, and 0.71 is chosen for the mass transfer calculations when compared with experimental corrosion rates. The turbulent diffusivity D_t of each species j varies within the domain as turbulent viscosity μ_T varies through the VSL (Davies, 1972).

2.2. Velocity and eddy distribution in straight tubes

In a turbulent flow, momentum is usually transferred by viscosity and velocity fluctuations. The analogy of eddy diffusion of momentum is used to define the turbulent diffusion of mass and is given by Eq. (5) (Lin et al., 1953):

$$D_t = \left(\frac{y^+}{C}\right)^3 \frac{\mu}{\rho} \qquad (5)$$

Where the constant C ranges from 8.9 to 14.5 (Davies, 1972; Lin et al., 1953). y^+ is the dimensionless distance from the wall calculated using Eq. (6):

$$y^+ = \frac{y u_\tau \rho}{\mu} \qquad (6)$$

And,

$$u^+ = \frac{u}{u_\tau} \qquad (7)$$

$$u_\tau = \sqrt{\frac{\tau_w}{\rho}} \qquad (8)$$

Where u^+ is the dimensionless velocity (m/s), u is the average velocity (m/s), y is the vertical distance from the wall (m), u_τ is the frictional velocity (m/s), and τ_w is the wall shear stress of fluid (Pa).

Davies (1972) provided an empirical correlation shown using Eq. (9) to calculate the VSL thickness (δ) as a function of the Reynolds number and the diameter of the pipe, assuming that the edge of the VSL is at $y^+ = 5$.

$$\delta = 25 \, Re^{-7/8} d \qquad (9)$$

This correlation is based on the empirical friction factor equation for zero pressure gradient flow. It assumed $y^+ = 5$ at the edge of the VSL, which has been found to depend on the turbulence intensity. Some studies found an average VSL thickness of $y^+ = 6.17$, questioning the validity of Eq. (9) (Popovich and Hummel, 1967).

Some researchers have used Eq. (9) for the VSL thickness and Eq. (10) for the turbulent diffusivity to predict the corrosion rate in pipe flow in the presence of a corrosion product film with a thickness δ_f (Nordsveen et al., 2003; Nesic et al., 2001).

$$D_t = \begin{cases} 0 & \text{for } y < \delta_f \\ 0.18\left(\frac{y - \delta_f}{\delta - \delta_f}\right)^3 \frac{\mu}{\rho} & \text{for } y > \delta_f \end{cases} \qquad (10)$$

There are several other empirical expressions which can be used (Notter and Sleicher, 1971; Rosen and Tragardh, 1995; Wang and Nesic, 2003) and can be applied to a specific set of experimental conditions (Nordsveen et al., 2003; Nesic et al., 2001; Kahyarian and Nesic, 2020;

Davies, 1972; Lin et al., 1953; Wang and Nesic, 2003). Therefore, to make these predictions more robust, CFD will be used to provide accurate velocity distributions required for corrosion rate predictions.

2.3. Computational fluid dynamics modelling

A 2D axisymmetric pipe with a steady-state, isoviscous, isothermal and incompressible flow is used for the simulations. COMSOL Multiphysics v5.5® is used to solve the governing equations given below (COMSOL, 2016).

The continuity equation:

$$\nabla \cdot \boldsymbol{u} = 0 \tag{11}$$

Where $\boldsymbol{u}$ is the velocity vector (m/s).

The conservation of momentum equation is given by Eq. (12):

$$\rho(\boldsymbol{u} \cdot \nabla)\boldsymbol{u} = -\nabla p + \nabla \cdot \left\{ (\mu + \mu_T)\left[\nabla \boldsymbol{u} + (\nabla \boldsymbol{u})^T\right] \right\} \tag{12}$$

Where p is the pressure (Pa).

The shear stress transport (SST) k-ω turbulence model is used for its ability to resolve the flow in the VSL and buffer layers (Owen et al., 2019). The turbulent viscosity (μ_T) in the SST k-ω model is calculated using Eq. (13):

$$\mu_T = \frac{\rho a_1 k}{\max(a_1 \omega, S f_{v2})} \tag{13}$$

Where k is the turbulent kinetic energy (m^2/s), ω is the specific turbulent dissipation rate (1/s), a_1 is a model constant with a value of 0.31, S is the mean strain-rate tensor and f_{v2} is a blending function.

2.4. Axisymmetric pipe model

2.4.1. 1D model of mass transfer in a pipe

This section describes mass transfer modelling in an axisymmetric pipe with an overview of the computational domain used, initial and boundary conditions, numerical method and mesh convergence study. Fig. 3 shows the computational domain used for the prediction of CO$_2$ corrosion in pipelines.

2.4.2. Initial and boundary conditions

It is assumed that all species are thoroughly mixed by turbulence and uniform concentrations of species is considered for the initial and boundary conditions. For the species not involved in the electrochemical reactions at the metal surface zero flux ($N_j = 0$) is specified, while for the others the flux is specified by:

$$N_j = -\frac{i_j}{n_j F} \tag{14}$$

Where i_j is the partial current of a specific electrochemical reaction which contributes to the overall current density, n_j is the number of moles of electrons exchanged per mole of species j, and F is Faradays constant (96,485 C/mol).

2.4.3. Numerical method

The VSL obtained from the CFD model is divided into a number of finite volumes (FVs) as shown in Fig. 3. There are a total of nFV finite volumes across the VSL with a total of nFV+1 flux boundaries. Each FV has an upstream and downstream flux boundary. Eq. (1) can be rewritten as:

$$\frac{\partial c_j}{\partial t} = f(c_j) \tag{15}$$

And integrating over the ith FV leads to:
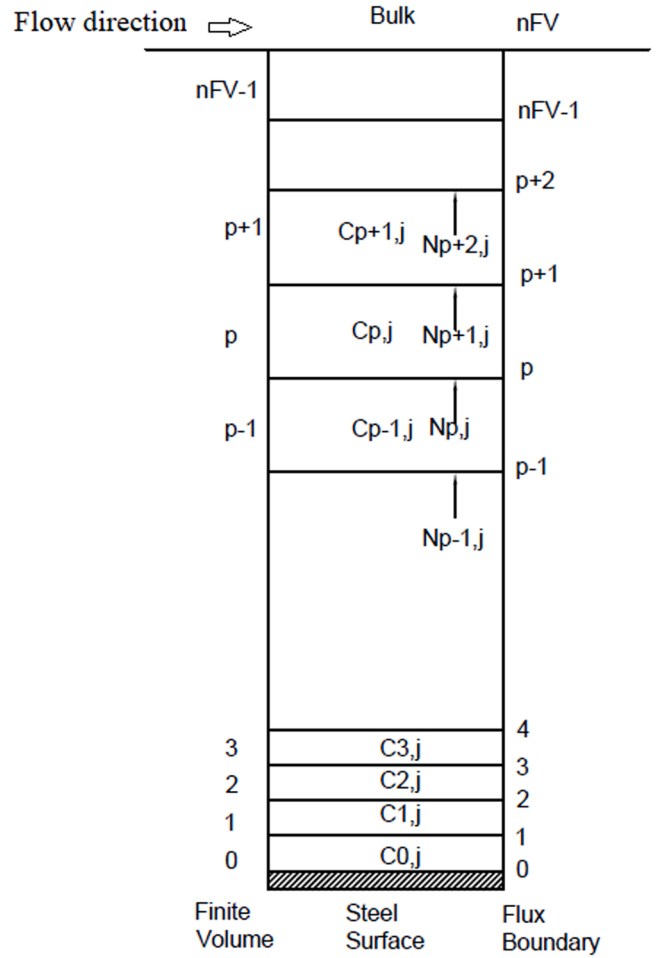
Fig. 3. Computational grid and finite volumes for discretising the computational domain. The fluxes of species are computed on the finite volume boundaries, and concentrations and potential of species are calculated at the centre of the finite volumes.

$$\frac{\partial c_j}{\partial t}\bigg|_i = f_j(c)|_i \; \frac{-N_{i,j} + N_{i+1,j}}{\Delta x_i} + R_{j,i} \tag{16}$$

Where $N_{i,j}$ is the flux of the jth species over the ith flux boundary, $N_{i+1,j}$ is the flux of the jth species over the $(i+1)$th flux boundary and $R_{j,i}$ is the rate of generation of species j in ith FV.

The backward Euler method computes the approximations using Eq. (17):

$$c_j^{n+1} = c_j^n + \Delta t \, f\left(c_j^{n+1}, t^{n+1}\right) \tag{17}$$

Where $f(c_j^{n+1})$ is the time derivative of the concentrations c_j at $(n+1)$th time step.

Here computing of c_j^{n+1} from c_j^n requires the solution of Eq. (18):

$$c_j^{n+1} - \Delta t \, f\left(c_j^{n+1}, t^{n+1}\right) = c_j^n \tag{18}$$

Eq. (18) is turned into a root finding problem and Newton's method is implemented to solve it. Consider v^i be the ith Newton iterate approximation of c^{n+1} and $v_{old} = c^n$. Fig. 4 shows the flow chart for the numerical method used for the corrosion rate predictions. At each time step, an iterative matrix equation is solved for $\Delta v = v^{i+1} - v^i$ subject to a specified error tolerance on the magnitude of Δv, starting from $v^0 =$

$v_{old} = c^n$.

Numerical calculations are carried out using the Python programming language. All the terms except those associated with the flux of species are calculated at the centre of the FV. The flux of species is calculated at the finite volume boundaries (Nordsveen et al., 2003).

These equations are solved subject to charge balance equations for FV 1 to $nFV-1$ (i.e. not adjacent to the corroding surface).

$$\Delta c^{H^+} + 2\Delta c^{Fe^{2+}} - \Delta c^{HCO_3^-} - 2\Delta c^{CO3^{2-}} - \Delta c^{OH^-} + \Delta c^{Na^+} - \Delta c^{Cl^-} = 0 \tag{19}$$

This is done by replacing the equation for the Δc^{H^+} freedom in FV 1 to $nFV-1$, with Eq. (19).

The conditions that the concentrations in the final FV, $nFV-1$, equal those calculated from the bulk steady state analysis, are imposed by setting $\Delta c_j = 0$ for all concentrations freedoms in the final FV, $nFV-1$.

2.4.4. Mesh convergence study for the mass transfer model

A mesh convergence study was carried out to determine the sensitivity to the number of FVs used for the prediction of CO_2 corrosion at pH 4, velocity 1 m/s, p_{CO_2} 1 bar and temperature 20 °C. The corrosion rate obtained for $nFV=25$ is 0.756,3 mm/yr which decreases to 0.752,2 mm/yr for $nFV=50$ and stays effectively constant for $nFV \geq 50$, as shown in Fig. 5. Hence, $nFV=50$ is used in all corrosion predictions given below.

2.5. CFD model of flow in an axisymmetric pipe

2.5.1. Geometry

Reynolds averaged Navier-Stokes (RANS) formulations can compute the flow field required for the computational domain shown in Fig. 3. The axisymmetric pipe model is used to reduce computational time without compromising accuracy. The pipe diameter D is equal to 15 mm (Radius $R = 7.5$ mm) with a length of 100 diameters (200 R) as the pipe length is chosen to obtain a fully developed flow at the outlet. The flow is simulated for Reynolds numbers ranging between 18,316 and 171,795 by changing the inlet velocity. The axisymmetric pipe model is shown in Fig. 6.

2.5.2. Initial and boundary conditions

The velocity inlet and pressure outlet boundary conditions are used for the simulations. A flow velocity from 1 to 10 m/s was specified at the inlet with a fluid density $\rho = 998$ kg/m³ and dynamic viscosity $\mu = 0.001$ Pa·s. The values of kinetic energy k and specific dissipation rate ω are specified at the inlet as $0.003,75$ m²/s² and 11.18 1/s respectively. Table 1 describes the boundary conditions used for the simulation.

2.5.3. Numerical method

COMSOL Multiphysics® (COMSOL, 2016) is based upon the finite element method (FEM) in which the field variables, in this case, u, p, k and ω are expressed using piecewise continuous basis functions on the discretised number of elements (de Boer et al., 2018). A form used for the approximation of a field variable φ is given using Eq. (20):
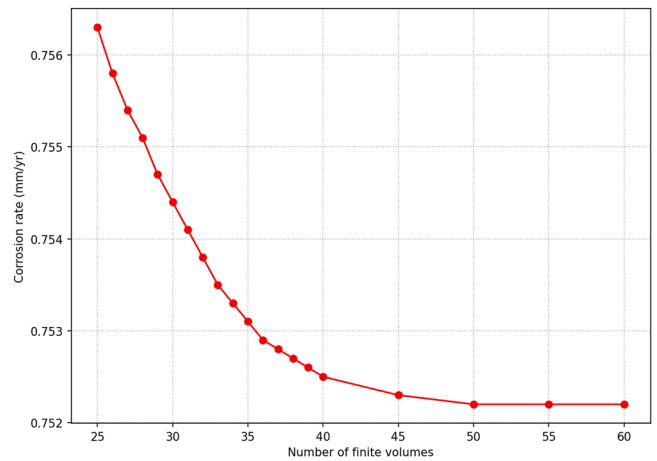
Fig. 5. Mesh convergence study for mass transfer model of corrosion prediction at pH = 4, velocity = 1 m/s, temperature = 20 °C, p_{CO_2} = 1 bar and diameter of pipe = 0.015 m.
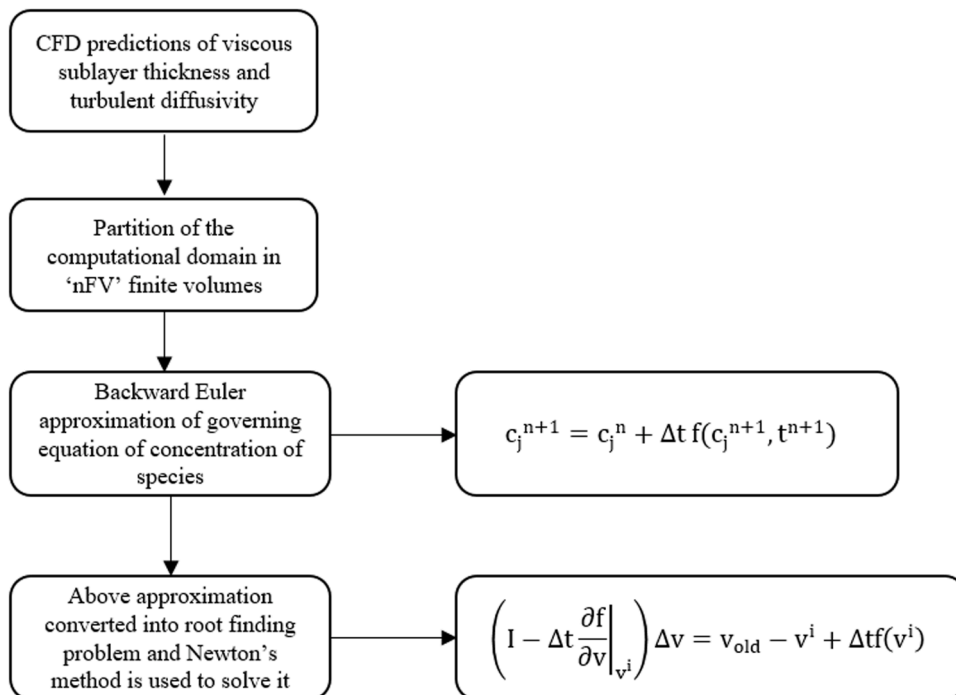
Fig. 4. Flow chart for the numerical method used for the corrosion rate predictions.
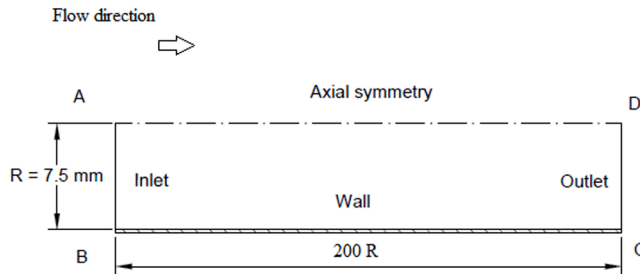
Fig. 6. The axisymmetric computational domain used for the simulation (diameter = 15 mm).

$$\varphi(x) = \sum_{i=1}^{n} \varphi_i N_i \tag{20}$$

Where φ_i are the nodal values of the variable and N_i denotes the basis function (de Boer et al., 2018). A weighted integral (Galerkin) approach (Hysing, 2012) is then used to generate the FEM equations. The weak form of this formulation to obtain the discrete nodal equation for a field variable φ is shown using Eq. (21):

$$\int_{x_i}^{x_{i+1}} \mathscr{L}(\varphi)N_i(x)\mathrm{d}x = \int_{x_i}^{x_{i+1}} sN_i(x)\mathrm{d}x \tag{21}$$

Where $\mathscr{L}(\varphi) = s$ is the strong form of the nodal equations. More details related to this can be found elsewhere (COMSOL, 2016; de Boer et al., 2018; Hysing, 2012).

2.5.4. Mesh convergence study for the CFD model

A structured quadrilateral mesh is used for the flow domain with rectangular boundary elements adjacent to the wall. The mesh adjacent to the wall should be fine enough to accurately predict the fluid flow in the VSL. The dimensionless distance y^+ to the centre of the element adjacent to the wall was chosen to be 0.1. The mesh convergence study was conducted to assess the impact of the number of mesh elements on

Table 1
Boundary conditions used for the simulation.

Boundary	Description	p	u	k	ω
AB	Inlet	$n\cdot\nabla p = 0$	$u = u_{in}$	$k = k_{in}$	$\omega = \omega_{in}$
CD	Outlet	$p = 0$	$n\cdot\nabla u = 0$	$n\cdot\nabla k = 0$	$n\cdot\nabla \omega = 0$
AD	Symmetry axis	$n\cdot\nabla p = 0$	$n\cdot\nabla u = 0$	$n\cdot\nabla k = 0$	$n\cdot\nabla\omega = 0$
BC	Pipe wall	$n\cdot\nabla p = 0$	$u = 0$	$k = 0$	$\omega = 0$
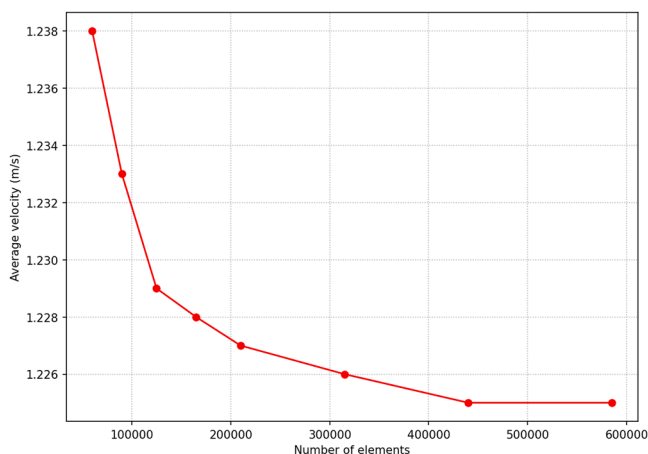
Fig. 7. Mesh convergence study for numerical simulations of axisymmetric pipe of diameter 0.015 m.

Table 2
VSL thickness predictions comparison between CFD and empirical correlation.

Velocity (m/s)	Reynolds number, Re	Empirical VSL δ (mm)	CFD VSL δ (mm)	Percentage difference
1	18,316	0.069,8	0.078,9	11.51%
2	35,686	0.039,0	0.045,6	14.52%
3	52,899	0.027,6	0.032,9	15.97%
4	70,019	0.021,6	0.025,5	15.44%
5	87,053	0.017,9	0.021,6	17.50%
6	104,138	0.015,3	0.017,9	14.80%
7	121,072	0.013,4	0.015,7	14.54%
8	138,079	0.011,9	0.013,9	14.39%
9	155,123	0.010,8	0.012,9	16.77%
10	171,795	0.009,8	0.011,8	16.53%
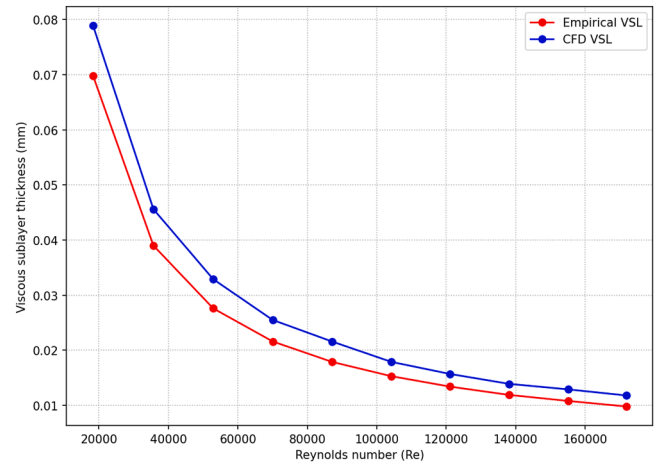
Fig. 8. VSL thickness comparison between empirical and CFD values for Reynolds number between 18,316 and 171,795.

the flow velocity at the outlet. The number of elements varied along the pipe length for the mesh convergence study is shown in Fig. 7. The average velocity at the outlet did not change significantly for > 440,000 mesh elements. Hence, to save computational time and power without compromising accuracy, the mesh with 440,000 elements was chosen for the simulations.

3. Results and discussion

3.1. Prediction of turbulent boundary-layer profiles

The values of the VSL thickness from the CFD are compared with the empirical correlation given by Eq. (9) for Reynolds numbers between 18,316 and 171,795, corresponding to the Reynolds number range in the experimental dataset used below. As shown in Table 2 and Fig. 8, the agreement is reasonably good, with the percentage difference between the two predictions ranging between 11.51 and 17.50. Note that the empirical correlation in Eq. (9) is obtained by curve fitting using the friction factor obtained by Blasius for Re in the range between 3,000 and 100,000. Davies (1972) assumed that $y^+ = 5$ at the edge of VSL, whereas Popovich and Hummel (1967) disputed this assumption as they had found that the average thickness of VSL was $y^+ = 6.2$ and proposed that it was most likely to be around $y^+ = 4.3$. These uncertainties in using the Davies (1972) empirical correlation can explain the discrepancy between the two sets of predictions shown in Table 2 and Fig. 8.

Fig. 9 compares the turbulent diffusivity profile obtained from CFD and the empirical Eq. (10) within the VSL thickness for $Re = 18,316$. The difference between the shapes of the two profiles can be linked with the approximate constants obtained by fitting the experimental data for the empirical correlation (Notter and Sleicher, 1971). The value of D_t
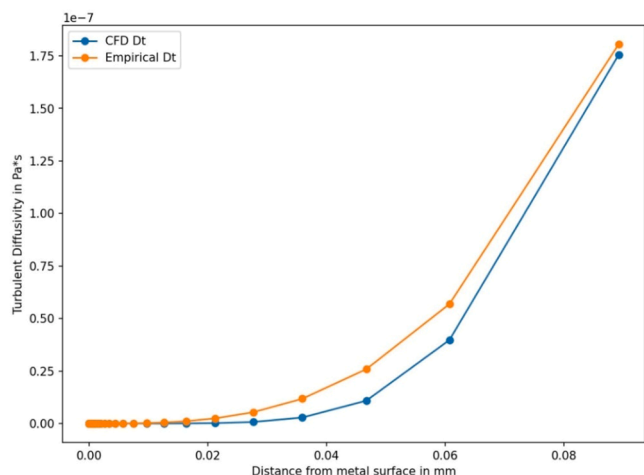
Fig. 9. Turbulent diffusivity comparison between CFD and empirical correlation for $Re = 18,316$.

depends on the VSL thickness hence, there is again an error in predicted values of D_t.

The values of VSL thickness and turbulent diffusivity profiles are then coupled with the mass transfer model to predict corrosion rates described in the following subsection.

3.2. Verification of corrosion rate predictions

Fig. 10 shows the concentration profiles for dissolved species for pH = 4, velocity = 1 m/s, temperature = 20 °C, $p_{CO_2} = 1$ bar and diameter of pipe = 0.015 m. At the metal surface, direct reduction and dissociation of carbonic acid results in depletion of H_2CO_3 species there, with a consequent increase in the concentration of HCO_3^-.

The corrosion rates shown here are a function of significant parameters such as pH, Reynolds number, p_{CO_2} and temperature. The experimental data is obtained using potentiodynamic sweeps for a diameter of 15 mm, temperature of 20 °C and p_{CO_2} of 1 bar (Nesic et al., 1995).

Figs. 11, 12 and 13 show the corrosion rates for pH 4 to 6 at different

Reynolds numbers for conditions in the absence of protective corrosion product formation. As the Reynolds number increases, the corrosion rate increases for each pH value. The effect of increasing the flow speed and therefore turbulence is to enhance the transport of species to and from the steel surface. At pH 4, there is a noticeable increase in the corrosion rate as the Reynolds number increased due to the presence of a much higher concentration of H^+ ions and enhanced transport of electrochemically active species towards and away from the metal surface. Conversely, at pH 5 and pH 6, the observed corrosion rate is much less than that at the pH 4.

The CFD-driven mass transfer model predictions are compared with those based on the set of empirical correlations, the experimental dataset of Nesic et al. (1995), and the numerical model of Srinivasan (2015) for pH between 4 and 6, velocities between 1 m/s and 10 m/s, with a temperature of 20 °C, $p_{CO_2} = 1$ bar and diameter of 0.015 m. The error bars on the experimental data are largest for pH 4, and it can be seen that each of the models is in reasonably good agreement with the experimental error bars for this case. Note that for pH 4 the corrosion rate predictions are particularly sensitive to the choice of electrochemical reaction rate constants, the precise values of which have been the subject of significant debate, see e.g., Nordsveen et al. (2003), Al-Khateeb et al. (2018), and Hu et al. (2018). Further sensitivity studies into the effects of the electrochemical reaction rate constants would be beneficial for pH values of 4 and below.

However for the cases of pH 5 and 6, with much smaller error bars, it can be seen clearly that the new CFD-driven model is far superior to either the empirical or the Srinivasan (2015) model and the limitations of the empirical approach are abundantly clear. For pH 5 and 6 typical discrepancies between the CFD-driven predictions and experimental data are only around 5%. This accuracy provides strong evidence that improving the modelling of flow in the VSL is very beneficial for mass-transfer based corrosion models and motivation to validate the approach for more complex, practically relevant corrosion scenarios.

4. Conclusion

A novel, CFD-driven modelling methodology for predicting CO_2 corrosion rates in pipelines is proposed. CFD based on the SST k-ω model, with its proven ability to resolve near-wall flow regions
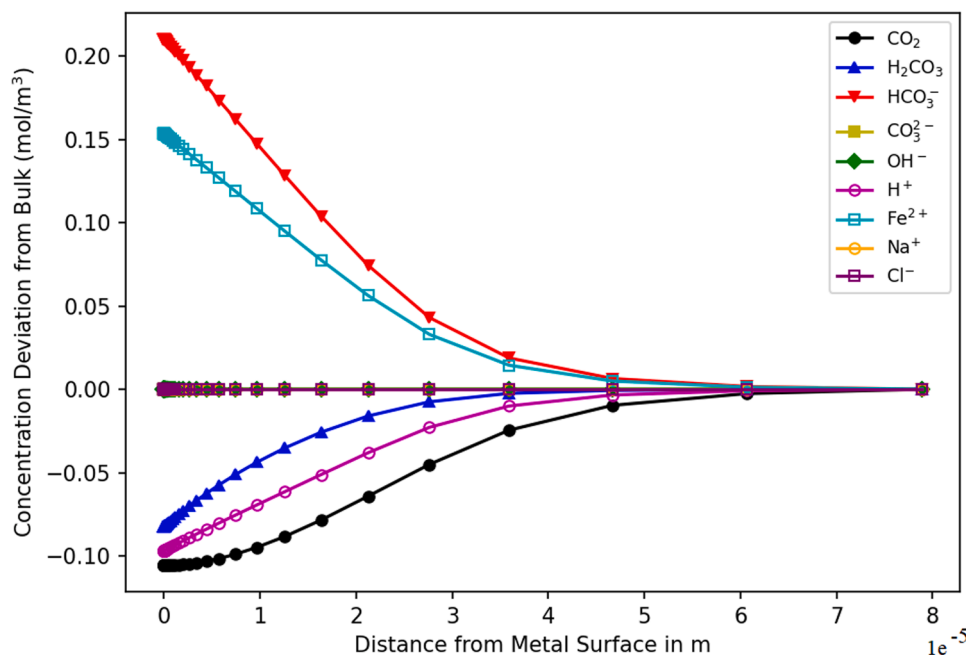
Fig. 10. Concentration deviation of dissolved species from the values in bulk at for pH = 4, velocity = 1 m/s, temperature = 20 °C, $p_{CO_2} = 1$ bar and diameter of pipe = 0.015 m.
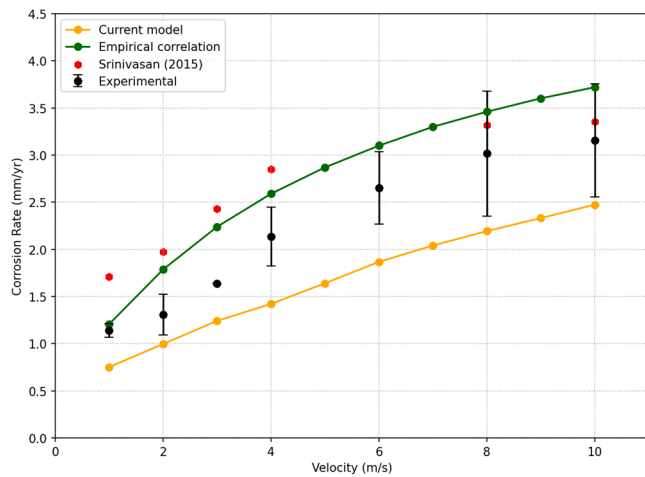
Fig. 11. CO_2 corrosion rate predictions for pH = 4, temperature = 20 °C, p_{CO_2} = 1 bar and diameter = 0.015 m and its comparison with model based on empirical correlations of VSL and D_t, experimental data of Nesic et al. (1995), and numerical model of Srinivasan (2015).
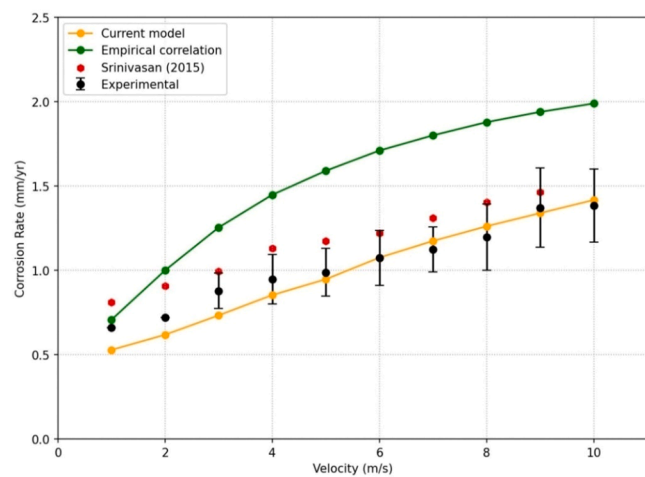
Fig. 12. CO_2 corrosion rate predictions for pH = 5, temperature = 20 °C, p_{CO_2} = 1 bar and diameter = 0.015 m and its comparison with model based on empirical correlations of VSL and D_t, experimental data of Nesic et al. (1995), and numerical model of Srinivasan (2015).
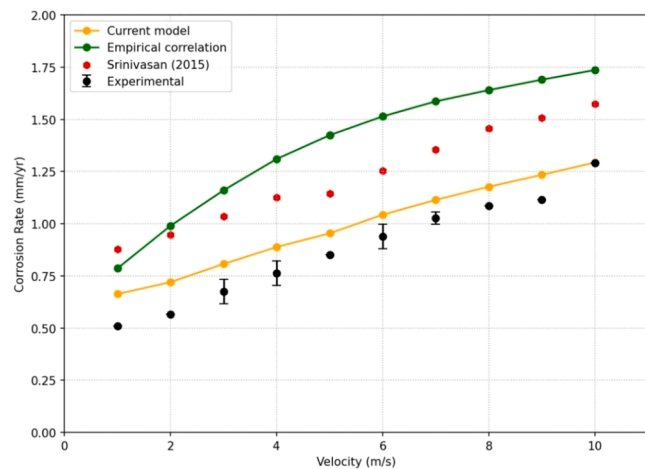
Fig. 13. CO_2 corrosion rate predictions for pH = 6, temperature = 20 °C, p_{CO_2} = 1 bar and diameter = 0.015 m and its comparison with model based on empirical correlations of VSL and D_t, experimental data of Nesic et al. (1995)), and numerical model of Srinivasan (2015).

accurately, is used to provide accurate predictions of the VSL thickness and turbulent diffusivities, which are then used within a mass transfer model of aqueous CO_2 corrosion. This new approach leads to significantly improved predictions of corrosion rate over a range of conditions and provides strong evidence that improving the modelling of flow in the VSL is very beneficial for mass-transfer based corrosion models. It also shows clearly that the current approach of using empirical models to predict VSL and associated turbulent diffusivities is both inaccurate and restrictive.

The key advantage of the new approach is its flexibility. It provides a firm, scientific foundation for predicting corrosion rates by determining VSL and flow conditions in much more complex, and practically relevant, situations. The approach now needs further validation in such scenarios.

The present model is developed for application to cases with high electrolyte conductivity and low temperatures, for which electro-migration and $FeCO_3$ corrosion product formation can both be neglected. Since the goal of the paper is to assess the benefits of determining the VSL conditions accurately, it is beneficial to avoid corrosion product formation conditions as this obviates the need for introducing additional empiricism into the corrosion model. However, if required, the model presented here can be extended to account for electro-migration by the addition of the term $z_j u_j F c_j \nabla \varphi$ in Eq. (3) whereas the inclusion of $FeCO_3$ corrosion product formation on the metal surface will necessitate a time-dependant solution scheme similar to those developed in references (Nordsveen et al., 2003; Nesic et al., 2001). Finally, note that the electrochemical reaction rate constants can have a strong influence on corrosion rate predictions, particularly for lower pH values (Nordsveen et al., 2003; Al-Khateeb et al., 2018; Hu et al., 2018). It would therefore also be useful to carry out a systematic investigation into their influence on corrosion rate predictions, for example using machine-learning methods. This approach is becoming increasingly popular in CFD-based simulations (Brunton et al., 2020).

Data availability

The raw/processed data required to reproduce these findings cannot be shared at this time as the data also forms part of an ongoing study.

CRediT authorship contribution statement

Udayraj Thorat: Funding acquisition, Conceptualization, Data curation, Methodology, Software, Writing – original draft. **Michael Jones:** Data curation, Software, Writing – review & editing. **Richard Woollam:** Supervision, Writing – review & editing. **Joshua Owen:** Writing – review & editing. **Richard Barker:** Funding acquisition, Conceptualization, Methodology, Supervision, Writing – review & editing. **Harvey Thompson:** Funding acquisition, Conceptualization, Data curation, Methodology, Software, Supervision, Writing – review & editing. **Gregory de Boer:** Funding acquisition, Conceptualization, Methodology, Software, Supervision, Writing – review & editing.

Declaration of Competing Interest

The authors declare that they have no known competing financial interests or personal relationships that could have appeared to influence the work reported in this paper.

Acknowledgment

Appendix

A.1 Water chemistry modelling

Carbon dioxide (CO_2) when dissolved in water creates the chemical species called carbonic acid (H_2CO_3). The carbonic acid then dissociates to give bicarbonate ions (HCO_3^-). The bicarbonate ions are further dissociated, giving carbonate (CO_3^{2-}) and hydrogen ions. Table A.1 shows chemical reactions related to this equilibrium (Nordsveen et al., 2003; Nesic et al., 2001).

Table A.1
Chemistry of CO_2 dissociation in water.

Chemistry of CO_2 dissociation	Reaction	Equilibrium constant
Carbon dioxide dissolution	$CO_{2(g)} \rightleftharpoons CO_{2(aq)}$	$K_{sol} = \dfrac{CO_{2(aq)}}{pCO_{2(g)}}$
Carbon dioxide hydration	$CO_{2(aq)} + H_2O_{(l)} \rightleftharpoons H_2CO_{3(aq)}$	$K_{hyd} = \dfrac{[H_2CO_3]}{[CO_{2(aq)}]}$
Dissolution of carbonic acid	$H_2CO_{3(aq)} \rightleftharpoons HCO_{3aq}^- + H_{(aq)}^+$	$K_{ca} = \dfrac{[HCO_3^-][H^+]}{[H_2CO_3]}$
Dissolution of bicarbonate ion	$HCO_{3aq}^- \rightleftharpoons CO_3^{2-}(aq) + H_{(aq)}^+$	$K_{bi} = \dfrac{[CO_3^{2-}][H^+]}{[HCO_3^-]}$
Dissociation of water	$H_2O_{(l)} \rightleftharpoons OH_{(aq)}^- + H_{(aq)}^+$	$K_w = [OH^-][H^+]$

The reaction rates depend on the temperature, p_{CO_2} and ionic strength (Nordsveen et al., 2003). Table A.2 provides the equilibrium constants used in the corrosion prediction model. The forward reaction rate constants are denoted as K_f and backward reaction rate constants are represented as K_b. T_f is the temperature in degrees Fahrenheit, T_c is the temperature in degrees Celsius, T is the temperature in Kelvin, I is the ionic strength, and p is pressure in psi.

Table A.2
Equilibrium constants used in the corrosion prediction model.

Equilibrium constants	Refs.
$K_{sol} = \dfrac{14.5}{1.00258} \times 10^{-(2.27+0.00565\ T_f - 8.06\times10^{-6}\ T_f^2 + 0.075\ I)}\ \dfrac{molar}{bar}$	Oddo et al. (1982)
$K_{hy} = 0.00258$	Palmer and Van Eldik (1983)
$K_{f,hy} = 10^{329.85 - 110.541 \times\ \log_{10}(T_k) - (17265.4/T_k)}\ s^{-1}$	Palmer and Van Eldik (1983)
$K_{ca} = 387.6 \times 10^{-(6.41 - 1.594\times10^{-3}\ T_f + 8.52\times10^{-6}\ T_f^2 - 3.07\times10^{-5}\ p - 0.4772\ I^{0.5} + 0.118\ I)}\ molar$	Oddo et al. (1982)
$K_{f,ca} = 10^{5.71 + 0.0526\ T_c - 2.94\times10^{-4}\ T_c^2 + 7.91\times10^{-7}\ T_c^3}\ s^{-1}$	Bamford and Tiffer (1972)
$K_{bi} = 10^{-(10.61 - 4.97\times10^{-3}\ T_f + 1.331\times10^{-5}\ T_f^2 - 2.624\times10^{-5}\ p - 1.166\ I^{0.5} + 0.3466\ I)}\ molar$	Oddo et al. (1982)
$K_{f,bi} = 10^9\ s^{-1}$	Nordsveen et al. (2003)
$K_{wa} = 10^{-(29.3868 - 0.0737549\ T_k + 7.47881\times10^{-5}\ T_k^2)}\ (molar)^2$	Kharaka et al. (1988)
$K_{b,wa} = 7.85 \times 10^{10}\ (molar)^{-1}(s)^{-1}$	Delahay (1952)

Table A.3
Equations for the calculation of reaction rates.

Reaction	Reaction rate equation
Dissolution of carbon dioxide	$R_{CO_{2,s}} = \dfrac{\partial}{\partial t}(c_{CO_{2,s}}) = K_{b,hy}\ c_{H_2CO_{3,s}} - K_{f,hy} c_{CO_{2,s}}$
Formation of carbonic acid (H_2CO_3)	$R_{H_2CO_{3,s}} = \dfrac{\partial}{\partial t}(c_{H_2CO_{3,s}}) = -(K_{b,hy}\ c_{H_2CO_{3,s}} - K_{f,hy} c_{CO_{2,s}}) - (K_{f,ca}\ c_{H_2CO_{3,s}} - K_{b,ca} c_{H_s^+} c_{HCO_{3,s}^-})$
Formation of bicarbonate ions (HCO_3^-)	$R_{HCO_{3,s}^-} = \dfrac{\partial}{\partial t}(c_{HCO_{3,s}^-}) = (K_{f,ca}\ c_{H_2CO_{3,s}} - K_{b,ca} c_{H_s^+} c_{HCO_{3,s}^-}) - (K_{f,bi}\ c_{HCO_{3,s}^-} - K_{b,bi} c_{H_s^+} c_{CO_{3,s}^{2-}})$
Formation of carbonate ions (CO_3^{2-})	$R_{CO_{3,s}^{2-}} = \dfrac{\partial}{\partial t}(c_{CO_3^{2-}}) = (K_{f,bi}\ c_{HCO_{3,s}^-} - K_{b,bi} c_{H_s^+} c_{CO_{3,s}^{2-}})$
Formation of hydroxide ions (OH^-)	$R_{OH^-} = \dfrac{\partial}{\partial t}(c_{OH_s^-}) = K_{f,wa} - K_{b,wa} c_{H_s^+} c_{OH_s^-}$
Formation of H^+ ions	$R_{H_s^+} = \dfrac{\partial}{\partial t}(c_{H_s^+}) = (K_{f,ca}\ c_{H_2CO_{3,s}} - K_{b,ca} c_{H_s^+} c_{HCO_{3,s}^-}) + (K_{f,bi}\ c_{HCO_{3,s}^-} - K_{b,bi} c_{H_s^+} c_{CO_{3,s}^{2-}}) + (K_{f,wa} - K_{b,wa} c_{H_s^+} c_{OH_s^-})$

The equations presented in Table A.3 are solved for the prediction of concentrations of species c_j, where j is used as an index for the species involved in the corrosion process. The representation of the concentration of species c_j is given below:

$$c = \left[c_{CO_{2,s}}, c_{H_2CO_{3,s}}, c_{HCO_{3,s}^-}, c_{CO_3^{2-}}, c_{OH_s^-}, c_{H_s^+} \right] \tag{A.1}$$

$$c_j = c(j)$$
$$j = 1, 2, \cdots, N \tag{A.2}$$

Where N is the total number of species involved in the corrosion process.

B. Electrochemical reactions

The nature of the CO_2 corrosion observed in oil and gas industries is electrochemical (Nesic et al., 1995). Table B.1 shows all the electrochemical reactions that take place in the current mass transfer model of CO_2 corrosion prediction, which includes the reduction of H^+ and H_2CO_3. The other cathodic reduction reaction such as reduction of HCO_3^- becomes important only at high pH conditions in CO_2-rich solutions due to increase in concentrations of bicarbonate ions as pH increases (Gray et al., 1989). The corrosion rate decreases steadily with the increase in pH in range 4 to 7 while bicarbonate ions concentration increases highlighting the insignificance of HCO_3^- reduction. The evolution of hydrogen due to the dissociation of water is found to be significant only at $p_{CO_2} \ll 1$ and $pH > 5$ which is less practical in CO_2 corrosion situations (Nordsveen et al., 2003). Hence reduction of HCO_3^- and H_2O is ignored from the current mass transfer model. The model is structured so that the additional cathodic reactions can be switched on and off.

Table B.1
Electrochemical reactions take place on the metal surface.

Electrochemical reaction	Reaction type
$2H^+_{(aq)} + 2e^- \rightleftharpoons 2H_{2(g)}$	Cathodic
$2H_2CO_{3(aq)} + 2e^- \rightleftharpoons 2HCO^-_{3aq} + 2H_{2(g)}$	Cathodic
$Fe^{2+}_{(aq)} + 2e^- \rightleftharpoons Fe_s$	Anodic

The reaction rate of these electrochemical reactions is expressed in terms of an electrical current density given by Eq. (B.1).

$$i = \pm i_0 \times 10^{\pm \frac{E - E_{rev}}{b}} \tag{B.1}$$

Where i_0 is the exchange current density with the positive sign for anodic reaction and negative sign for cathodic reactions, E is the electrical potential of the surface, E_{rev} is the reversible potential, and b is the Tafel slope constant. Nesic et al. (2001) and Nordsveen et al. (2003) suggested that i_0 and E_{rev} are nonlinear functions of the species concentration in a reaction. i_0 is calculated using Eq. (B.2):

$$i_0 = i_{0ref} \left(\frac{c_{H^+}}{c_{H^+ref}} \right)^{a_1} \left(\frac{c_{CO_2}}{c_{CO_2 ref}} \right)^{a_2} \left(\frac{c_{H_2CO_3}}{c_{H_2CO_3 ref}} \right)^{a_3} e^{-\frac{\Delta H}{R} \left(\frac{1}{T} - \frac{1}{T_{ref}} \right)} \tag{B.2}$$

Where i_{0ref} is the reference exchange current density, c_{H^+} is the concentration of H^+ ions at the surface, c_{H^+ref} is the reference concentration of H^+ ions, c_{CO_2} is the concentration of CO_2 species at the surface, $c_{CO_2 ref}$ is reference concentration of CO_2 species, $c_{H_2CO_3}$ is the concentration of H_2CO_3 at the surface, $c_{H_2CO_3 ref}$ is the reference concentration of H_2CO_3, a_{1-3}, are the power constants, ΔH is the activation energy, and T_{ref} is the reference temperature. The values for these constants are available for both cathodic reactions (Nesic et al., 1995) and anodic reactions (Nesic and Thevenot, 1996). Table B.2 shows the values of electrochemical reaction rate constants for cathodic reactions used in different corrosion prediction models.

Table B.2
Electrochemical reaction rate constants for electrochemical reactions (Nordsveen et al., 2003; Nesic et al., 2001; Al-Khateeb et al., 2018).

Electrochemical reaction	$i_{0,ref}$ (a/m^2)	a_1	$c_{H^+,ref}$ (mol /L)	a_2	$c_{CO_2,ref}$ (mol /L)	a_3	$c_{H_2CO_3,ref} \left(\frac{mol}{L} \right)$	$\Delta H \left(\frac{KJ}{mol} \right)$	T_{ref}(°C)	E_{rev} (V)	b(V)
Hydrogen evolution	0.05	0.5	10^{-4}	0	N/A	0	N/A	30	25	$-\frac{2.303\,RT}{F} pH$	$\frac{2.303\,RT}{0.5F}$
Carbonic acid reduction	0.06	-0.5	10^{-5}	0	N/A	1	10^{-4}	50	20	$-\frac{2.303\,RT}{F} pH$	$\frac{2.303\,RT}{0.5F}$
Iron dissolution	1	2 if pH < 4 1 if $4 \leq$ pH < 5 0 if pH$\geq$5	10^{-4}	1 for $p_{CO_2} \leq 1$ bar 0 for $p_{CO_2} > 1$ bar	0.0366	0	N/A	37.5	25	-0.488	$\frac{2.303\,RT}{1.5F}$

C. The SST k-ω turbulence model

This section describes the equation used in the SST k-ω model for use in CFD (COMSOL, 2016). The equations used in the SST k-ω models are given by Eq. (C.1):

$$\rho \frac{\partial k}{\partial t} + \rho \cdot \nabla k = P - \rho \beta_0^* k \omega + \nabla \cdot [(\mu + \sigma_k \mu_T) \nabla k] \tag{C.1}$$

$$\rho \frac{\partial \omega}{\partial t} + \rho \boldsymbol{u} \cdot \nabla \omega = \frac{\rho \gamma}{\mu_T} P - \rho \beta \omega^2 + \nabla \cdot [(\mu + \sigma_\omega \mu_T) \nabla \omega] + 2(1 - f_{v1}) \frac{\rho \sigma_{\omega^2}}{\omega} \nabla \omega \cdot \nabla k \tag{C.2}$$

$$P = \min\left(P_k, 10 \rho \beta_0^* k \omega\right) \tag{C.3}$$

Where P_k is the production term given as:

$$P_k = \mu_T \left\{ \nabla \boldsymbol{u} : \left[\nabla \boldsymbol{u} + (\nabla \boldsymbol{u})^T \right] - \frac{2}{3} (\nabla \cdot \boldsymbol{u})^2 \right\} - \frac{2}{3} \rho k \nabla \cdot \boldsymbol{u} \tag{C.4}$$

The turbulent viscosity is given by Eq. (C.5),

$$\mu_T = \frac{\rho a_1 k}{\max(a_1 \omega, S f_{v2})} \tag{C.5}$$

Where S is the characteristic magnitude of the mean velocity gradients,

$$S = \sqrt{2 S_{ij} S_{ij}} \tag{C.6}$$

The constants in the model are defined through interpolation of inner and outer values:

$$\phi = f_{v1} \phi_1 + (1 - f_{v1}) \phi_2 \text{ for } \phi = \beta, \gamma, \sigma_k, \sigma_\omega \tag{C.7}$$

Where f_{v1} and f_{v2} are interpolation functions defined as:

$$f_{v1} = \tanh(\theta_1^4) \tag{C.8}$$

$$\theta_1 = \min\left[\max\left(\frac{\sqrt{k}}{\beta_0^* \omega l_\omega}, \frac{500\mu}{\rho \omega l_\omega^2}\right), \frac{4\rho \sigma_{\omega^2} k}{CD_{k\omega} l_\omega^2}\right] \tag{C.9}$$

$$CD_{k\omega} = \max\left(\frac{2\rho \sigma_{\omega^2}}{\omega} \nabla \omega \cdot \nabla k, 10^{-10}\right) \tag{C.10}$$

$$f_{v2} = \tanh(\theta_2^2) \tag{C.11}$$

$$\theta_2 = \max\left(\frac{2\sqrt{k}}{\beta_0^* \omega l_\omega}, \frac{500\mu}{\rho \omega l_\omega^2}\right) \tag{C.12}$$

Where l_ω is the distance closest to the wall. The default values of constants are $\beta_1 = 0.075$, $\beta_2 = 0.0828$, $\gamma_1 = \frac{5}{9}$, $\gamma_2 = 0.44$, $\sigma_{k1} = 0.85$, $\sigma_{k2} = 1.0$, $\sigma_{\omega1} = 0.5$, $\sigma_{\omega2} = 0.856$, $\beta_0^* = 0.09$, $a_1 = 0.31$

The SST k-ω model is a low-Reynolds model. As the no-slip boundary condition is imposed, values of $\boldsymbol{u}$ and k become zero at the wall. The boundary condition for ω is given by Eq. (C.13):

$$\lim_{l_\omega \to 0} \omega = \frac{6\mu}{\rho \beta_1 l_\omega^2} \tag{C.13}$$

To obtain an accurate solution it is required that,

$$l_\omega^+ = \frac{\rho u_\tau l_\omega}{\mu} \sim 1 \tag{C.14}$$

D. Species properties as a function of temperature

Table D.1
Species properties as a function of temperature used in the mass transfer model (Haynes et al., 2014).

Property	Equation
Density	$\rho(T) = 1152.3 - 0.5116\,T$
Dynamic viscosity	$\mu(T) = \mu_{\text{ref}} \times 10^{\frac{1.3272(20-T)-0.001053(20-T)^2}{T+105}}$
Diffusion coefficient	$D = D_{\text{ref}}\left(\frac{T}{T_{\text{ref}}}\right)\left(\frac{\mu_{\text{ref}}}{\mu}\right)$

Where T_{ref} is the reference temperature $= 20\ °C$, $\mu_{\text{ref}} = 1.002$ kg/(m.s).

E. Molecular diffusion coefficients
Table E1

Table E.1
Reference values of molecular diffusion coefficients of chemical species involved in the corrosion process.

Species	Diffusion coefficients (m^2/s)	Refs.
CO_2	1.96×10^{-9}	Perry and Green (1987)
H_2CO_3	2×10^{-9}	Kvarekval (1997)
HCO_3^-	1.105×10^{-9}	Newman (1991)
CO_3^{2-}	0.92×10^{-9}	Kvarekval (1997)
H^+	9.312×10^{-9}	Newman (1991)

Table E.1 (*continued*)

Species	Diffusion coefficients (m^2/s)	Refs.
OH^-	5.26×10^{-9}	Newman (1991)
Fe^{2+}	0.72×10^{-9}	Kvarekval (1997)

References

Abe, K., Kondoh, T., Nagano, Y., 1994. A new turbulence model for predicting fluid flow and heat transfer in separating and reattaching flow. 1: flow field calculations. Int. J. Heat Mass Transf. 37, 139–151.

Al-Khateeb, M., Barker, R., Neville, A., Thompson, H., 2018. An experimental and theoretical investigation of the influence of surface roughness on corrosion in CO_2 environments. J. Corros. Sci. Eng. 20, 84.

Balsara, N.P., Newman, J., 2021. Electrochemical Systems. John Wiley & Sons, Incorporated, Newark, United States. http://ebookcentral.proquest.com/lib/leeds/detail.action?docID=6478263.

Bamford, C.H., Tiffer, C.F.H., 1972. *Comprehensive chemical kinetics*, 6. Elsevier, Amsterdam.

Berger, F.P., Hau, K.F.F.L., 1977. Mass transfer in turbulent pipe flow measured by the electrochemical method. Int. J. Heat Mass Transf. 20, 1185–1194. https://doi.org/10.1016/0017-9310(77)90127-2.

Bozzini, B., Ricotti, M.E., Boniardi, M., Mele, C., 2003. Evaluation of erosion-corrosion in multiphase flow via CFD and experimental analysis. Wear 255, 237–245. https://doi.org/10.1016/S0043-1648(03)00181-9.

Brunton, S.L., Noack, B.R., Koumoutsakos, P., 2020. Machine learning for fluid mechanics. Annu. Rev. Fluid Mech. 52, 477–508. https://doi.org/10.1146/annurev-fluid-010719-060214.

COMSOL, 2016. COMSOL is a commerical software and they have recommended a citation style given as below, COMSOL Multiphysics® v. 6.1. COMSOL AB, Stockholm, Sweden. http://www.comsol.com.

COMSOL, CFD Module User's Guide, 2016. https://doc.comsol.com/5.3/doc/com.comsol.help.cfd/CFDModuleUsersGuide.pdf.

Davies, J.T., 1972. Turbulence Phenomenon. Academic Press New York and London.

de Boer, G.N., Johns, A., Delbosc, N., Burdett, D., Tatchell-Evans, M., Summers, J., Baudot, R., 2018. Three computational methods for analysing thermal airflow distributions in the cooling of data centres. Int. J. Numer. Method H. 28 (2), 271–288.

de Waard, C., Milliams, D.E., 1975. Carbonic acid corrosion of steel. Corrosion 31, 177–181.

de Waard, C., Craig, B.D., Smith, L.M., 2003. The influence of crude oils on well tubing corrosion rates. NACE - International Corrosion Conference Series.

Delahay, P., 1952. Implications of the kinetics of ionic dissociation with regard to some electrochemical processes-application to polarography. J. Am. Chem. Soc. 74, 3497–3500. https://doi.org/10.1021/ja01134a013.

El-Batsh, H.M., Doheim, M.A., Hassan, A.F., 2012. On the application of mixture model for two-phase flow induced corrosion in a complex pipeline configuration. Appl. Math. Model. 36, 5686–5699. https://doi.org/10.1016/j.apm.2012.01.017.

El-Gammal, M., Mazhar, H., Cotton, J.S., Shefski, C., Pietralik, J., Ching, C.Y., 2010. The hydrodynamic effects of single-phase flow on flow accelerated corrosion in a 90-degree elbow. Nucl. Eng. Des. 240, 1589–1598. https://doi.org/10.1016/j.nucengdes.2009.12.005.

Gray, L.G.S., Anderson, B.G., Danysh, M.J., Tremaine, P.R., 1989. Mechanisms of carbon steel corrosion in brines containing dissolved carbon dioxide at pH 4. Corrosion 1–19.

Halvorsen, A.M.K., Sontvedt, T., 1999. CO_2 corrosion model for carbon steel including a wall shear stress model for multiphase flow and limits for production rate to avoid mesa attack. Corrosion. San Antonio.

Haynes, W., Lide, D.R., Bruno, T.J., 2014. CRC Handbook of Chemistry and Physics, 95th ed. CRC Press.

Hu, H., Cheng, Y.F., 2016. Modeling by computational fluid dynamics simulation of pipeline corrosion in CO_2-containing oil-water two phase flow. J. Pet. Sci. Eng. 146, 134–141. https://doi.org/10.1016/j.petrol.2016.04.030.

Hu, H., Xu, H., Huang, C., Chen, X., Li, X., Li, Y., 2018. Numerical predictions of uniform CO_2 corrosion in complex fluid domains using low reynolds number models. Metals 8. https://doi.org/10.3390/met8121001 (Basel).

Hysing, 2012. Mixed element FEM level set method for numerical simulation of immiscible fluids. J. Comput. Phys. 231, 2449–2465. https://doi.org/10.1016/j.jcp.2011.11.035.

Jepson, W.P., Bhongale, S., Gopal, M., 1996. Predictive model for sweet corrosion in horizontal multiphase slug flow. NACE Int. Corros. Conf. Ser. 1996-March.

Kahyarian, A., Nesic, S., 2020. On the mechanism of carbon dioxide corrosion of mild steel: experimental investigation and mathematical modeling at elevated pressures and non-ideal solutions. Corros. Sci. 173, 108719 https://doi.org/10.1016/j.corsci.2020.108719.

Kanwar, S., 1994. Study and Modelling of Sweet Corrosion of Multiphase Mixtures in Horizontal Pipelines. Ohio University.

Keating, A., Nesic, S., 2000. Numerical prediction of erosion-corrosion in bends. Corrosion, 2000.

Kharaka, Y.K., Gunter, W.D., Aggarwal, P.K., 1988. A Computer Program For Geochemical Modeling of Water-Rock Interactions. California.

Kvarekval, J., 1997. A kinetic model for calculating concentration profiles and fluxes of CO_2-related species across the Nernst diffusion layer. Corrosion. Corrosion. New Orleans, Louisiana.

Li, H., Woollam, R., 2012. Mechanistic modelling of flow enhanced corrosion in complex geometry. In: Proceedings of the NACE International Corrosion Conference Series.

Li, Q., Hu, H., Cheng, Y.F., 2016. Corrosion of pipelines in CO_2-saturated oil-water emulsion flow studied by electrochemical measurements and computational fluid dynamics modeling. J. Pet. Sci. Eng. 147, 408–415. https://doi.org/10.1016/j.petrol.2016.09.011.

Lin, C.S., Moulton, R.W., Putnam, G.L., 1953. Mass transfer between solid wall and fluid streams - Mechanism and eddy distribution relationships in turbulent flow. Ind. Eng. Chem. 45, 636–640. https://doi.org/10.1021/ie50519a048.

Lv, W., Ou, G., Liu, X., Gong, C., 2020. Experimental and numerical studies on the corrosion properties of AISI 316L stainless steel in two-phase upward slug flows. Eng. Appl. Comput. Fluid Mech. 14, 897–909. https://doi.org/10.1080/19942060.2020.1780155.

Nešić, S., Li, H, Huang, J., Dusan, S., 2009. An open source mechanistic model for CO_2/H_2S corrosion of carbon steel. CORROSION paper No. 09572.

Nešić, S., Kahyarian, A., Choi, Y.S., 2019. Implementation of a comprehensive mechanistic prediction model of mild steel corrosion in multiphase oil and gas pipelines. Corrosion 75, 274–291. https://doi.org/10.5006/3093.

Nešić, S., 2007. Key issues related to modelling of internal corrosion of oil and gas pipelines - a review. Corros. Sci. 49, 4308–4338. https://doi.org/10.1016/j.corsci.2007.06.006.

Nesic, S., Thevenot, N., 1996. Electrochemical Properties of Iron Dissolution in the Presence of CO_2- basics revisited. NACE Int. Annu. Conf. Expo.

Nesic, S., Postlethwaite, J., Olsen, S., 1995. An electrochemical model for prediction of corrosion of mild steel in aqueous carbon dioxide solutions. Corrosion 52, 280–294. https://doi.org/10.5006/1.3293640.

Nesic, S., Nordsveen, M., Nyborg, R., Stangeland, A. A mechanistic model for CO_2 corrosion with protective iron carbonate films, (2001).

Newman, J.S., 1991. Electrochemical Systems. Prentice Hall, Englewood Cliffs, N.J.

Nordsveen, M., Nešić, S., Nyborg, R., Stangeland, A., 2003. A mechanistic model for carbon dioxide corrosion of mild steel in the presence of protective iron carbonate films - part 1: theory and verification. Corrosion 59, 443–456. https://doi.org/10.5006/1.3277576.

Notter, R.H., Sleicher, C.A., 1971. The eddy diffusivity in the turbulent boundary layer near a wall. Chem. Eng. Sci. 26, 161–171. https://doi.org/10.1016/0009-2509(71)86088-8.

Oddo, J.E., Tomson, M.B., JPT, J., 1982. Simplified calculation of $CaCO_3$ saturation at high temperatures and pressures in brine solutions. Pet. Technol. 34, 1583–1590. https://doi.org/10.2118/10352-PA.

Olsen, S., 2003. CO_2 Corrosion prediction by use of the Norsok M-506 model - guidelines and limitations. Corrosion 1–12.

Owen, J., Godfrey, J., Ma, W., de Boer, G., Al-Khateeb, M., Thompson, H., Neville, A., Ramsey, C., Barker, R., 2019. An experimental and numerical investigation of CO_2 corrosion in a rapid expansion pipe geometry. Corros. Sci., 108362 https://doi.org/10.1016/j.corsci.2019.108362.

Palmer, D.A., Van Eldik, R., 1983. The chemistry of metal carbonato and carbon dioxide complexes. Chem. Rev. 83, 651–731. https://doi.org/10.1021/cr00058a004.

Perry, R.H., Green, D.W., 1987. Perry's Chemical Engineers' Handbook, 50th ed. McGraw-Hill, New York.

Pietralik, J.M., 2012. The role of flow in flow-accelerated corrosion under nuclear power plant conditions. J. Adv. Maint. 4, 63–78.

Popovich, A.T., Hummel, R.L., 1967. Experimental study of the viscous sublayer in the pipe flow. AIChE J. 13, 854–860.

Prasad, M., Gopika, V., Sridharan, A., Parida, S., 2018. Pipe wall thickness prediction with CFD based mass transfer coefficient and degradation feedback for flow accelerated corrosion. Prog. Nucl. Energy 107, 205–214. https://doi.org/10.1016/j.pnucene.2018.04.024.

Rosen, C., Tragardh, C., 1995. Prediction of turbulent high Schmidt number mass transfer a low Reynolds number k–E turbulence model using. Chem. Eng. J. 59, 153–159.

Sanchez-Caldera, L.E., Griffith, P., Rabinowicz, E., 1988. The mechanism of corrosion-erosion in steam extraction lines of power stations. J. Eng. Gas Turbines Power 110, 180–184. https://doi.org/10.1115/1.3240099.

Srinivasan, V., 2015. Evaluation of Flow Coupled CO_2 Corrosion Using CFD: kinetics & Hydrodynamics. NACE Int. Corros. Conf. Ser. 1–15.

Stephens, L.I., Mauzeroll, J., 2019. Demystifying mathematical modeling of electrochemical systems. J. Chem. Educ. 96, 2217–2224. https://doi.org/10.1021/acs.jchemed.9b00542.

Tang, P., Yang, J., Zheng, J., Wong, I., He, S., Ye, J., Ou, G., 2009. Failure analysis and prediction of pipes due to the interaction between multiphase flow and structure. Eng. Fail. Anal. 16, 1749–1756. https://doi.org/10.1016/j.engfailanal.2009.01.002.

Tominaga, Y., Stathopoulos, T., 2007. Turbulent Schmidt numbers for CFD analysis with various types of flowfield. Atmos. Environ. 41, 8091–8099. https://doi.org/10.1016/j.atmosenv.2007.06.054.

Wang, S., Nesic, S., 2003. On coupling CO_2 corrosion and multiphase flow models. NACE CORROSION. Athens, Ohio. p, 03631.

Wang, K., Li, C., Li, Y., Lu, J., Wang, Y., Luo, X., 2020. A fully coupled model of hydrodynamic-chemical-electrochemical processes for CO_2 uniform corrosion in multi-physics environment. J. Pet. Sci. Eng. 193 https://doi.org/10.1016/j.petrol.2020.107436.

Wang, W., Sun, Y., Wang, B., Dong, M., Chen, Y., 2022. CFD-based erosion and corrosion modeling of a pipeline with CO_2-containing gas–water two-phase flow. Energies. 15 https://doi.org/10.3390/en15051694.

Wang, F., 1999. Modelling of Aqueous CO_2 Corrosion of Iron in Turbulent Pipe Flow. University of Saskatchewan.

Yeoh, G.H., Tu, J., 2010. Computational techniques for multiphase flows. Butterworth-Heinemann, Oxford.

Zhang, G.A., Cheng, Y.F., 2010. Electrochemical characterization and computational fluid dynamics simulation of flow-accelerated corrosion of X65 steel in a CO_2-saturated oilfield formation water. Corros. Sci. 52, 2716–2724. https://doi.org/10.1016/j.corsci.2010.04.029.

Zheng, D., He, X., Che, D., 2007. CFD simulations of hydrodynamic characteristics in a gas-liquid vertical upward slug flow. Int. J. Heat Mass Transf. 50, 4151–4165. https://doi.org/10.1016/j.ijheatmasstransfer.2007.02.041.

Zheng, Y., 2015. Electrochemical Mechanism and Model of H_2S Corrosion of Carbon Steel. Ohio University.